



Cite this: *Nanoscale*, 2017, 9, 17494

Embedded nanoparticle dynamics and their influence on switching behaviour of resistive memory devices†

S. Tappertzhofen  ‡ and S. Hofmann  *

Resistively switching Conductive Bridge Random Access Memories (CBRAMs) rely on the controlled formation and dissolution of metallic filaments within a solid insulator, and are emerging building blocks for beyond von Neumann computing architectures and neuromorphic computing. A lack of understanding of the underlying switching mechanisms currently prevents further device utilisation and optimisation. We present a study of lateral and vertical CBRAM model devices that allow us to systematically relate important switching properties and their statistics to a direct characterisation of their critical switching region by scanning and transmission electron microscopy, *i.e.* to the physical nature of metal filaments and inclusions on all relevant length scales. We find that filaments are composed of metallic clusters and show how filament dynamics link to migration effects of embedded nanoparticles under voltage bias stress. The formation of metal clusters is promoted by a dynamic interplay of cation mobility and redox rate during switching. These clusters are not completely removed from the switching material matrix upon RESET and appear to grow by consumption of smaller clusters. We discuss in detail the interfacial stress of the nanoparticles in the context of their interaction with the switching material and ambient atmosphere. This allows us to consistently interpret previous literature and to suggest future device improvements.

Received 8th August 2017,
Accepted 29th October 2017

DOI: 10.1039/c7nr05847k

rsc.li/nanoscale

Introduction

Resistive random access memory (RRAM) has emerged as one of the select technologies for emerging non-volatile memory in the semiconductor roadmap¹ that enables fast read/write times combined with long data retention.² Its basic two-terminal device structure with a switching material sandwiched between two metal electrodes can be implemented with a range of materials, including oxides commonly used in the industry,³ and hence readily lends itself to monolithic integration and back-end-of-line-processes.⁴ This enables beyond von Neumann computing architectures^{5–7} and ultra-low-power operation.⁸ Further, the device design can be adopted to serve as synaptic emulators for neuromorphic computing.^{9,10} While the device design is simple, the underlying switching mechanisms in RRAM are in fact far from simple, including thermal, chemical and electronic/electrostatic effects.³ A lack of detailed understanding currently prevents further device utilisation

and optimisation.^{11,12} A main class of RRAM devices are so called Conductive Bridge Random Access Memories (CBRAM, sometimes termed Electrochemical Metallization cells, ECM) for which the switching mechanism is based on the formation and dissolution of metallic filaments driven by cationic migration within a thin film (including oxides,¹³ *e.g.* Ta₂O₅ or SiO₂, iodides,¹⁴ polymers¹⁵ and higher chalcogenides¹⁶ like GeSe or GeS) between an active (usually Ag or Cu) and inert (usually Au or Pt) electrode.¹⁷ The classical understanding of such CBRAM devices is that they rely on a (usually single) continuous metal filament whereas a tunnel gap between the filament and one of the two electrodes dominates the device resistance.^{18,19} This simple view however fails to capture the physical origin of the statistical variability of CBRAMs,²⁰ degradation effects,²¹ and the interaction and stress¹⁹ conditions between a considerable large metal inclusion within a solid switching material. Recent more detailed studies using for instance scanning electron microscopy (SEM), transmission electron microscopy (TEM) (*e.g.* ref. 22–24) and nanoscale plasmon-enhanced spectroscopy²⁵ revealed that the filament nucleation position can differ from cycle to cycle and that the filament removal is often incomplete during RESET. *In situ* TEM showed dynamic metal nanoparticle agglomeration processes dictating the detailed switching behaviour.²⁶ This highlights the need for connecting such detailed atomistic pro-

Department of Engineering, Electrical Engineering Division, University of Cambridge, CB3 0FA Cambridge, UK. E-mail: sh315@cam.ac.uk

† Electronic supplementary information (ESI) available: TEM and SEM characterisation as well as Weibull plots and statistical analysis. See DOI: 10.1039/c7nr05847k

‡ Now at aixACCT Systems GmbH, Talbotstraße 25, 52068 Aachen, Germany.

cesses much more directly to the switching behaviour of realistic CBRAM geometries that show stable resistance levels and that are cycled many times in application relevant conditions.

Here we study lateral and crossbar CBRAM model devices that allow us to systematically relate important switching properties and their statistics to a direct characterisation of their critical switching region by SEM and TEM, *i.e.* to the physical nature of metal filaments and inclusions on all relevant length scales. We focus on silicon dioxide (SiO_2) and a PMMA (poly [methyl methacrylate]) as switching materials, as they are well studied and offer ease of fabrication. We analyse the switching by Weibull statistics and identify different limiting regimes which can be linked to multiple filament formation. Our electron microscopy analysis reveals that filaments are composed of metallic clusters rather than continuous metal nanowires. These clusters are not completely removed from the switching material matrix upon RESET and appear to grow by consumption of smaller clusters. The formation of clusters is thereby promoted by a dynamic interplay of the cation mobility and redox rate during switching. We discuss in detail the interfacial stress of these particles in the context of their interaction with the switching material and ambient atmosphere. This allows us to consistently interpret previous literature and to suggest future device improvements.

Experimental

We fabricated lateral polymer and oxide based CBRAM devices with a nanogap in between the Au (counter-) and Ag (active-) electrode in order to be compatible with electron microscopy. Devices for SEM studies were fabricated directly on Si wafers (Fig. 1a). Devices for TEM were patterned on suspended 50 nm thin Si_3N_4 windows. A schematic of a TEM sample is shown in Fig. 1b. Fig. 1c and d depict SEM and TEM images of a lateral CBRAM device on a suspended Si_3N_4 window, respectively. Besides lateral devices we also fabricated conventional vertical Au/ SiO_2 /Ag nano-crossbars for comparison (ESI Fig. S1†).

Fabrication of lateral devices for SEM studies

Lateral CBRAM devices for SEM studies were fabricated on Si wafers with a wet-thermally grown 280 nm thick SiO_2 layer. We used electron-beam (e-beam) lithography (with MicroChem PMMA A4 950K as resist) for patterning of the electrodes and switching material (acceleration voltage 80 kV, emission current 4 nA). At first, the Au electrode and Au probe needle pads were patterned and deposited by thermal evaporation of 5 nm Cr (evaporation speed $s = 0.1 \text{ nm s}^{-1}$) and 30 nm Au ($s = 0.1 \text{ nm s}^{-1}$). Subsequently, the Ag electrode was patterned and deposited by thermal evaporation ($s = 0.1 \text{ nm s}^{-1}$). In addition to the 30 nm thick Ag layer, a 20 nm thick Au layer was deposited on top of the Ag metal to prevent environmental degradation. For both electrodes, lift-off was done in acetone followed by 2-propanol. For PMMA as switching material we spin coated PMMA A4 950K (from MicroChem) at 5000 rpm and exposed only the needle pads with the electron-beam, so that

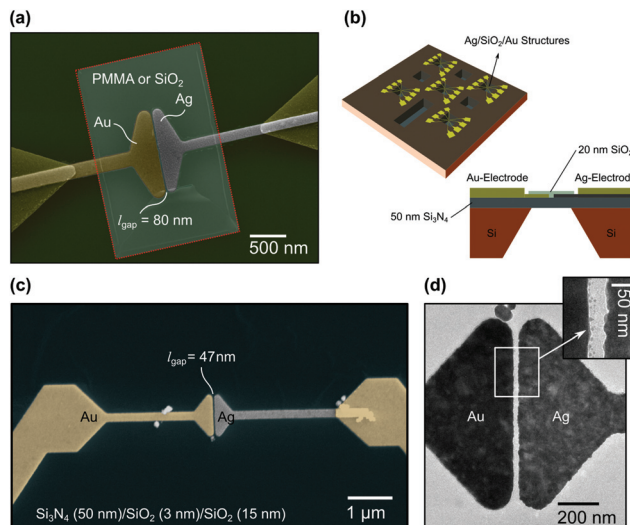


Fig. 1 Lateral CBRAM geometry analysed in this study. (a) SEM picture (in false colour) of a lateral Au/ SiO_2 /Ag device (both PMMA and SiO_2 based devices were fabricated). Here, the gap distance is $l_{\text{gap}} = 80 \text{ nm}$. (b) Schematic of a lateral device patterned on a suspended Si_3N_4 window for TEM studies (the side view is not to scale). (c) SEM picture (in false colour) and (d) TEM image of a device for TEM studies, respectively.

the switching area remained unexposed. Subsequently, the PMMA was developed for 10 s in methyl isobutyl ketone (MIBK, 1 : 3 in 2-propanol). In contrast, for SiO_2 based devices, the switching area was patterned by e-beam lithography followed by radio-frequency (RF) sputtering of 50 nm SiO_2 in Ar-atmosphere (pressure $4.6 \times 10^{-3} \text{ hPa}$, 5 W cm^{-2} , $s = 0.01 \text{ nm s}^{-1}$) and lift-off.

Fabrication of lateral devices for TEM studies

The fabrication process of devices for TEM studies is similar to that of the aforementioned fabrication steps. However, instead of simple Si wafers, we used commercially available suspended Si_3N_4 windows (50 nm thickness) on silicon wafers (EMResolutions, SN100-A50Q33). We found that the adhesion of PMMA is poor on the wafers, which, however, was significantly improved by RF sputtering a 3 nm thick SiO_2 layer (identical process parameters as above) prior to the first patterning step. Instead of using acetone we found that lift-off is improved by using *n*-methyl-2-pyrrolidone (NMP) followed by 2-propanol.

Fabrication of crossbar devices

Crossbar device fabrication is very similar to what is described for lateral SEM devices. At first, the 30 nm thick Au electrode is patterned and deposited (with a 5 nm thick Cr layer to improve the adhesion), followed by RF sputtering of the switching material (SiO_2 , thickness 7 nm, same process parameters as above) and thermal evaporation the 30 nm thick Ag top electrode (covered by a 30 nm thick Au protective layer). Between each step a lift-off in acetone and 2-propanol was done exploiting that the deposition by evaporation was found to be very anisotropic.

Electrical characterization and electron microscopy

A Keithley 4200-SCS Parameter Analyzer in a triaxial measurement configuration was used for electrical characterization. The system was controlled by a custom-made software to precisely setup the measurement conditions (*i.e.* fixed current range depending on the current compliance I_{CC} used, voltage range 200 V, delay factor 2.5, filter factor 0.6, and analogue-to-digital converter integration time 1.3 power cycles). These conditions allow adjusting a constant sweep rate of $\nu \approx 100 \text{ mV s}^{-1}$ (otherwise specified). We applied triangular voltage sweeps in ambient atmosphere at room temperature to study the switching behaviour of vertical and lateral devices. Thereby, the voltage is applied between the Ag and Au electrode with the Au electrodes grounded at all time. For both PMMA and SiO_2 based cells an electroforming step, *i.e.* a higher voltage (usually around 8 to 12 V for PMMA, and 8 to 14 V for SiO_2 , which depends on the gap width), for the first switching cycle of a pristine cell is required to enable resistive switching.¹⁷ After electroforming a smaller voltage (termed as switching or SET voltage, V_{SET}) is required to switch from the high resistive state (HRS) to the low resistive state (LRS). For PMMA devices we usually found $V_{\text{SET}} \approx 0.2 \text{ V}$ to 1 V, however, some samples show higher SET voltages $V_{\text{SET}} \approx 1 \text{ V}$ to 3 V. For SiO_2 based cells we found $V_{\text{SET}} \approx 0.4 \text{ V}$ to 1.5 V. A current compliance ($I_{CC} = 2 \mu\text{A}$, otherwise specified) is used to avoid damage of the cell in the low resistive ON state. The statistical variation of SET voltage was analyzed by Weibull statistics²⁷

$$F(x) = 1 - \exp \left[\left(-\frac{x}{x_0} \right)^\beta \right] \quad (1)$$

Here, F is the probability for a resistance transition from the high resistive state to the low resistive state for a given SET voltage, *i.e.* x corresponds to V_{SET} (for simplicity we define $x_0 = 1 \text{ V}$). When $\log((1 - F(x))^{-1})$ is plotted *versus* $\log(V_{\text{SET}})$ the Weibull slope β gives information about the physical processes determining the statistical probability for a given set of switching voltages.

After switching the devices were characterized by a FEI Philips XL30 sFEG SEM (5–15 kV acceleration voltage, spot size 3) and/or a FEI Philips Tecnai 20 TEM (200 kV acceleration voltage, spot size 3, objective aperture 70 μm). TEM images were further processed to identify isolated nanoparticles and to calculate their area/diameter and next nearest neighbour distance (see ESI Fig. S2[†]).

Results

Resistive switching characteristics

Fig. 2a shows a SEM picture of a Au/PMMA/Ag device (with gap distance of $l_{\text{gap}} = 80 \text{ nm}$) after 60 switching cycles. The switching curves are shown in the inset. At least two metal inclusions, marked as (2) and (3), can be identified in the gap with a diameter of about $\approx 100 \text{ nm}$ (up to $\approx 200 \text{ nm}$ at the Ag electrode interface). There is a third filament, marked (1),

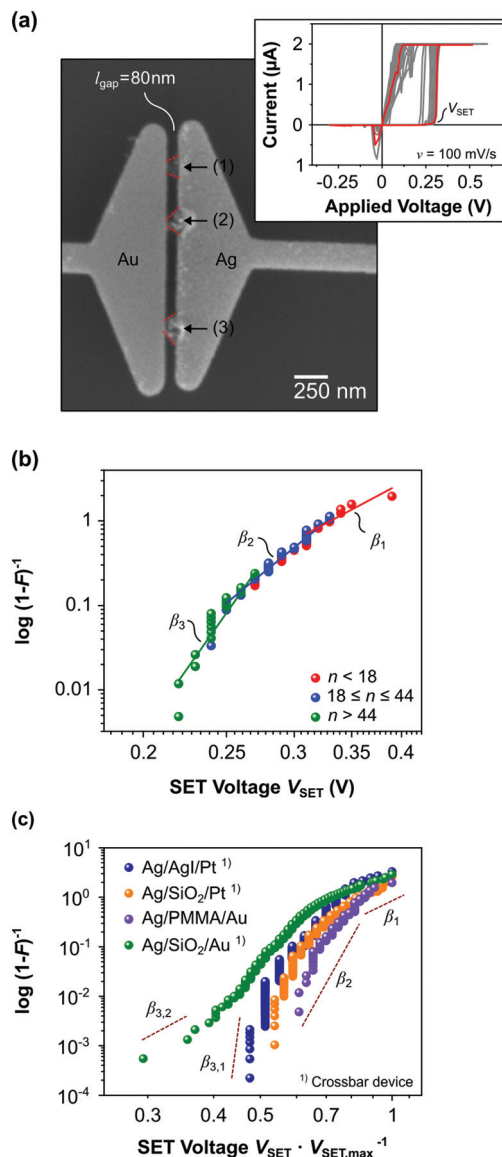


Fig. 2 Resistive switching of a Au/PMMA/Ag lateral CBRAM. (a) SEM image after 60 switching cycles. At least two ((2) and (3)) metal bridges can be identified (and a potential third one (1) is visible as well). The switching curves are shown in the inset (a typical curve is highlighted in red). A current compliance of $I_{CC} = 2 \mu\text{A}$ and a sweep rate of $\nu = 100 \text{ mV s}^{-1}$ were used. (b) Weibull statistics of the device shown in (a). The characteristics can be fit to at least two (potentially three) Weibull slopes $\beta_1 \approx 5$ for cycle $n < 18$ (red), $\beta_2 \approx 8$ for $18 \leq n \leq 44$ (blue), and $\beta_3 \approx 14$ for $n > 44$ (green) depending on the cycle number n . (c) Weibull statistics of various crossbar devices (in blue, yellow and green) and the lateral device from (b) (in purple). For comparison the switching voltage is normalized with the devices' individual maximum set voltage $V_{\text{SET,max}}$. The data for the Ag/AgI/Pt and Ag/SiO₂/Pt device is based on ref. 28 and 29, respectively. The data for the Ag/SiO₂/Au device is based the measurement shown in ESI Fig. S3.[†]

visible with smaller material contrast, potentially due to a smaller amount of Ag clusters forming the filament. A significant change of the Ag electrode morphology for filaments (2) and (3) is also observed. The growth of the Ag filament

appears to consume a significant amount of the active Ag electrode material.

The Weibull statistics²⁷ of the SET voltages are plotted in Fig. 2b. We can fit the characteristics to at least two (potentially three) Weibull slopes $\beta_1 \approx 5$ for cycle $n < 18$ (red), $\beta_2 \approx 8$ for $18 \leq n \leq 44$ (blue), and $\beta_3 \approx 14$ for $n > 44$ (green) depending on the cycle number n . In Fig. 2c, the Weibull statistics of several crossbar devices and the lateral device from Fig. 2b are plotted normalized with the individual maximum SET voltage $V_{\text{SET,max}}$ of the devices for comparison (*i.e.* for the device from Fig. 2b, $V_{\text{SET,max}} = 0.4$ V). For all devices, at least two slopes β_1 and β_2 (potentially three, with $\beta_{3,1}$ and $\beta_{3,2}$) can be identified. Thus, the statistical distribution of the switching voltage of the lateral and vertical devices are comparable.

Filament morphology

We find sub-20 nm filaments and features challenging to be analysed by SEM, and hence we fabricated Ag/SiO₂/Au devices on suspended Si₃N₄ windows for TEM analysis. Fig. 3a–e show TEM images of a device after 30 cycles. After switching (Fig. 3b) a region with a large amount of Ag particles is found (Fig. 3c) and another region with a small filament/small chain of particles (diameter about 10 nm) is shown in Fig. 3d. The lattice spacing 0.23 nm is consistent with Ag (111), see Fig. 3e and i. The Weibull statistics (shown in ESI Fig. S8†) reveal two Weibull slopes which appears consistent with the two filament regions we observe. The device has been switched OFF and then again switched ON once more (which would correspond

to cycle $n = 31$). The TEM image after this additional switching process is shown in Fig. 3f with a zoom into the two switching regions shown in Fig. 3g–i. For comparison, a SEM picture of the device after 31 cycles is shown in Fig. 3j.

The TEM analysis clearly shows that the filament here consists of an agglomeration of Ag nanoparticles with a size of $d \approx 3$ –50 nm in diameter. For simplicity, we assume a spherical shape for the particles although some (in particular those with larger diameters of more than 20 nm) differ from such ideal shape. Interestingly, the shape of the particles in both filament regions (Fig. 3c and d) has changed (Fig. 3g and h) after subsequent RESET and SET, and some particles seemed to have disappeared. We processed the TEM images (see ESI Fig. S2†) to extract the particle size d and their next nearest neighbour distance r for several devices (shown in ESI Fig. S9†). A data density (DD) graph summarizing all devices is shown in Fig. 4. We also plotted the average diameter and next nearest neighbour distance based on the Gaussian distributions calculated for the particles of each device. Note, we assume a stable Ag cluster diameter >1 nm (ref. 30) for image processing as smallest particle size. We also calculated particle size and distance for SEM and TEM images shown by Yang *et al.*²² Fig. 4 reveals a clear trend: the larger the particle on average, the larger it's next nearest neighbour distance on average.

A closer look on the geometry of nanoparticles at higher TEM resolution is shown in Fig. 5a. The corresponding line scale spectra (averaged over the rectangular area shown in Fig. 5a) and Fast Fourier transform (FFT) spectrum of the par-

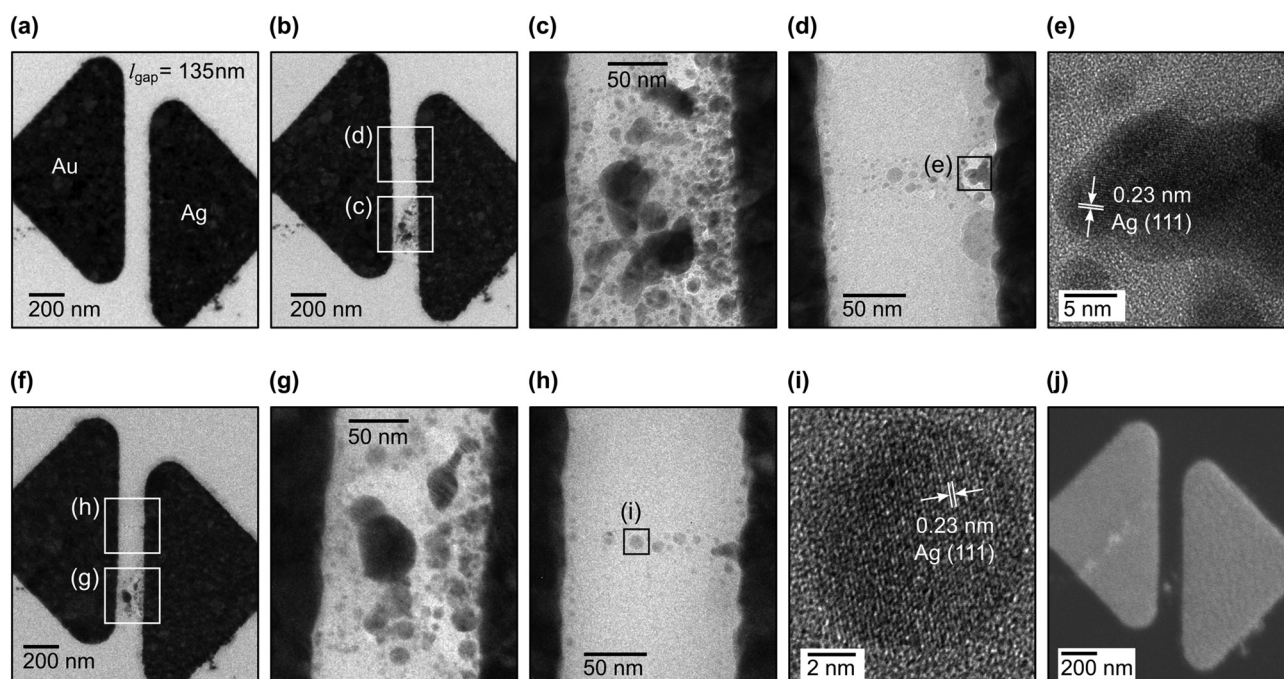


Fig. 3 TEM images (a)–(i) and a SEM image (j) of a Au/SiO₂/Ag lateral CBRAM before and after resistive switching of 30+ cycles. (a) The device before switching, and (b) the device after 30 cycles. (c) and (d) Zoom into the two filament regions of (b). (e) Zoom into the filament stub shown in (d) revealing a lattice spacing of 0.23 nm. (f)–(i) TEM image after a subsequent switch OFF/switch ON cycle (*i.e.* cycle $n = 31$). (j) SEM picture of the cell after 31 cycles.

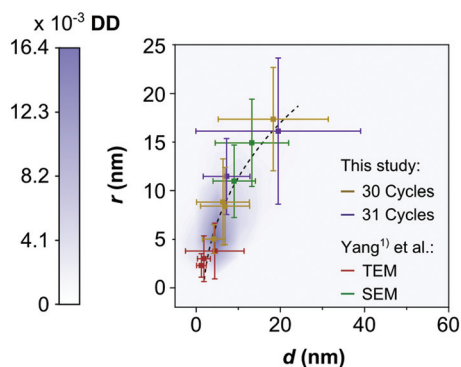


Fig. 4 Data density (DD) graph for the particle size d and their individual next nearest neighbour distance r . The colour bar indicates the density of data points (based on ESI Fig. S9†) at certain d and r values. The graph plots also the individual average particle diameter $\langle d \rangle$ and next nearest neighbour distance $\langle r \rangle$ for each device we analysed, compared to $\langle d \rangle$ and $\langle r \rangle$ values we calculated based on SEM and TEM images¹ published in a study²² by Yang *et al.* 1st and 2nd cycle indicate the $\langle d \rangle$ and $\langle r \rangle$ values we calculated for particles showed in Fig. 3c, d, g and h, respectively. The dotted black line indicates the trend between d and r , *i.e.* the larger the particle the larger the next nearest neighbour distance on average.

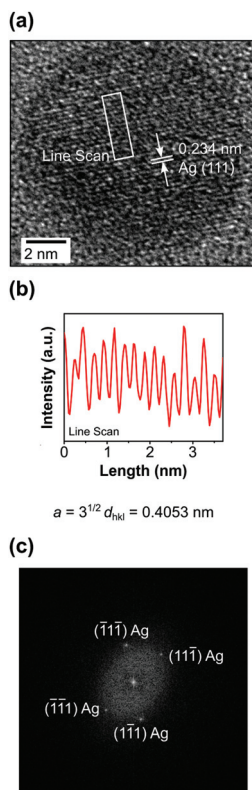


Fig. 5 TEM image of a Ag nanoparticle with high resolution. (a) The diameter of the nanoparticle is 11.8 nm. A line scan (b) reveals a lattice spacing of $d_{hkl} = 0.234$ nm which results in a lattice constant of $a \approx 0.405$ nm. This fits to the lattice spacing calculated from the diffraction peaks in the FFT spectrum (c) of the nanoparticle for the [110] zone axis.

article are shown exemplary in Fig. 5b and c, respectively. From the FFT spectrum we assign the spacing to Ag (111). The lattice spacing we get from the FFT spectra of several nanoparticles is in the range between $d_{hkl} = 0.219$ and 0.235 for Ag (111) giving a lattice constant of $a = 0.38$ –0.407 nm, with the average lattice constant $\langle d_{hkl} \rangle = 0.397$ nm \pm 0.0092 nm.

Discussion

Only little is known about the statistical variation of the switching properties and failure mechanisms for resistive memory devices and how these are linked. Accumulation of cations during switching leading to a decrease of the switching voltage²⁹ as well as a consumption of the active electrode material¹⁹ have been recently proposed. The different Weibull slopes we observe in Fig. 2b and c clearly highlight that the switching conditions can change during device operation (otherwise the statistical distribution would be characterized by only a single slope). In Fig. 2a we identify up to three different filaments. As the growth of only one filament at a time is very likely due to the field enhancement at the filament tip,³¹ we believe there is a high chance that the filaments were not formed simultaneously but in subsequent cycles. We thus attribute the three different slopes we observe to the three different filaments we identified by SEM. The quantitative value of the Weibull slope can be hard to estimate from the data as it is strongly affected by the dispersion of the SET voltages. We emphasise, however, that the quantitative slope itself is of minor importance in our study here. What is important is that the switching process clearly cannot be fitted in the Weibull diagrams (Fig. 2b and c) to a single linear slope.

Another example of multiple filaments and different Weibull slopes is shown in ESI Fig. S4,† while ESI Fig. S5† depicts a device with only one filament and one Weibull slope. Hence, we propose that the change of the switching condition is linked to the growth of another filament. That could be either: (I) a newly formed filament that has different switching properties, and/or (II) the switching conditions have changed in a way that the formation of a new filament is energetically more favourable and previously formed filaments become inactive. As we simultaneously observe degradation of the electrode interface in Fig. 2a (further examples are shown in ESI Fig. S7†), we believe (II) is more important as such degradation will most likely affect the local distribution of the electric field in the switching material. Such a degradation of the electrode by consumption of the electrode material has been predicted by Kinetic Monte Carlo simulations¹⁹ but so far it has not been directly experimentally observed. The multiple filaments and change of the filament position we observe in electron microscopy perfectly match to what we recently reported on in an *in situ* plasmon-enhanced spectroscopy study of vertical CBRAM crossbar devices.²⁵

In previous literature it has been observed that besides a single dominating filament other filament fragments can also grow during the forming process.²² If this situation is

assumed for Fig. 2, the three Weibull slopes would correspond to the respective individual filament that dominated the switching. The other filaments could be in-active and become dominating upon further switching similar to the aforementioned case (II). It is hence also possible that the stochastic nature of the switching is, at least partly, determined by the formation of multiple switching paths during forming that allow the growth of one dominating filament.

For lateral devices, we observed by SEM generally larger filament diameters (between 30–250 nm) than those expected in some vertical devices (*e.g.* 100–100 nm (ref. 2); vertical devices shown in ESI Fig. S1 and S3,† or sub-20 nm devices³²). A closer look by TEM (*e.g.* Fig. 3d) however reveals diameters in the order of some tens of nanometres and larger filaments consist of an accumulation of smaller filaments. Similar diameters of some tens of nanometres have been reported in previous studies.^{22,33}

From the SEM and TEM images the shape of the filaments (with more clusters close to the active electrode) suggests that the filaments grow from the active electrode towards the counter electrode. This is not consistent with the classical switching model where the cations are reduced at the counter electrode and a filament grows towards the active electrode.³⁴ It has been suggested that this alleged growth direction is a result of a complex interplay of the ion mobility and the redox rate:²⁴ low ion mobilities μ_i and low redox rates Γ^i of a particular ion species i (here $i = \text{Ag}^+$) result in dense filaments with their narrowest diameter at the counter electrode. Note, we suggest for non-classical electrolytes such as SiO_2 or PMMA the term *defect concentration* is more appropriate instead of *ion concentration*.

We observe the formation of discrete nanoparticles mainly in the vicinity of the active electrode, this would correspond to low μ_i and Γ^i , respectively.²⁴ In addition, a number of particles is also formed deep inside the switching material, and by further operation these particles appear to grow by consumption of smaller particles. In contrast, nucleation of rather large clusters in the switching material is, however, attributed by Yang *et al.* to low μ_i and high Γ^i .²⁴ We resolve this apparent discrepancy by proposing a spatial and time-variant dynamic interplay of the ion mobility and redox rate, rather than assuming constant values during device operation. Our model is schematically highlighted in Fig. 6. At the beginning of the switching event, the defect concentration is low and the redox rate is inhomogeneous across the switching material due to the deposition process and/or electroforming process. Due to weak cation–cation interactions, the low defect concentration results in high cation mobility compared to subsequent operation.^{35,36} A number of cations can migrate deep into the switching material and some get reduced due to dangling bonds or the local morphology in voids and holes (Fig. 6a). In a system where μ_i and Γ^i are considered to be constant in time, it is expected that the filament will be formed *via* nucleation of rather bulky and dense particles. However, as the defect concentration increases over time, the cation mobility is consequently reduced, promoting the formation of discrete nanoparticles close to the active electrode. In our case, nano-

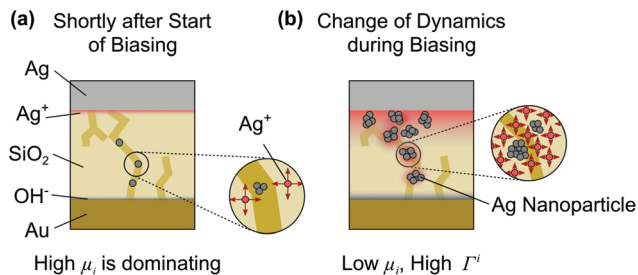


Fig. 6 Proposed schematic of the defect concentration affecting the ion mobility μ_i of ion species i (*e.g.* $i = \text{Ag}^+$). The dark yellow parts in the light-yellow switching material indicate potential morphological changes due to the forming process. At the beginning of a biasing experiment (a) the cation mobility may be high and dominating compared to the redox rate. A number of cations will be reduced in the switching material. During further biasing (b), the defect concentration nearby the metal clusters may increase to an extent where cation–cation interactions decrease the effective ion mobility (low μ_i) promoting the growth of rather bulky features in the switching material.

particles are formed both close to the active electrode and in the switching material, even for considerably long gap distances (see insets of ESI Fig. S9a, b and e†). The nanoparticles act as bipolar electrodes and can also locally supply cations by increasing the defect concentration in their vicinity. In addition, nearby larger nanoparticles may act as favourable reduction sides which effectively increases the local redox rate. Hence, during further device operation, we expect locally low μ_i and high Γ^i , resulting in further particle growth to rather bulky features in the switching material (Fig. 6b). We believe this dynamic interplay can explain the formation of nanoparticles in the switching material and nearby the active electrode, and simultaneously allows us to rationalize the growth of already formed larger nanoparticles by consumption of smaller particles.

During RESET instead of complete removal of the metal inclusions from the switching material, some larger particles may further consume smaller ones but remain in the switching material. Removal of those particles may be energetically more difficult due to the high local defect concentration (compared to the initial low concentration and thus now lower mobility) or a change of the local morphology (*e.g.* filling or formation of cracks and holes) of the switching material. This could also explain why some filaments remain inactive in the gap or grow from cycle to cycle due to further cation accumulation (exemplarily shown in ESI Fig. S6†). Removing these particles with even higher absolute negative voltages may however lead to damage of the cell, in particular of the insulator, and it becomes practically impossible to remove all particles in the gap. Apparently, this is a critical situation for the device endurance once a few particles become so large that the device cannot be switched OFF anymore. This requires a strategy to overcome the problem of non-removable particles. Doping the oxide matrix *e.g.* with fluorine may be a way to increase the OH^- concentration in the oxide as $\text{Si}(-\text{F})_2$ bonds are reported to increase the water absorption of SiO_2 .³⁷ A higher OH^- concentration at the electrodes enhances redox reactions during

RESET where counter ions are involved (typically OH^-).³⁸ Furthermore, higher water absorption (due to fluorine doping) may reduce the interfacial stress of particles embedded in the oxide (see discussion below).

Our data indicates that larger particles have larger next nearest neighbour distances on average (Fig. 4). This can be rationalised by electrochemical redox reactions (*i.e.* oxidation, dissolution, nucleation and reduction) between the metal particles/clusters (*e.g.* by interaction with mobile cations or counter charges) so that larger particles grow *via* the coalescence of smaller ones. When our results are put into context with Yang's data,²⁴ we find a similar relation between particle size and distribution. Ostwald ripening of metal particles in resistive switches has been previously discussed, *e.g.* in the context of electrochemical relaxation effects^{39,40} or the RESET process of unipolar switching devices.⁴¹ More recently, Wang *et al.* observed the agglomeration of Ag particles by *in situ* TEM.²⁶ The authors report that larger particles grow after bias stress by consumption of smaller particles and compared the diffusive behaviour to the accumulation and extrusion of Ca^{2+} cations in pre- and postsynaptic compartments. However, whereas Ostwald ripening is a thermodynamically-driven spontaneous process, we only observed a change of the particle shape during bias stress and did not observe any change without biasing even over several of weeks. The dominating process we observe is purely driven by external electrical bias. Nevertheless, we cannot exclude Ostwald ripening effects after bias stress with time constants of a few seconds or below. The growth of larger particles by consumption of smaller ones will further form particles remaining in the gap during RESET, as we believe it becomes more and more difficult to remove larger particles than smaller ones under negative bias stress. Furthermore, this ripening process may explain a low resistance stability problem highlighted in previous literature. In some cases instable ON states are observed for CBRAMs, especially for low and medium current compliances (typically well below 10 μA), see for instance ESI Fig. S10.† The origin of this instability has remained unclear to date. A unipolar RESET due to Joule assisted dissolution of the filament can be excluded for these low and medium currents. In contrast, we propose that an explanation is the coalescence of nanoparticles during filament growth. At first, nanoparticles are formed during switching and at some point they form a conductive bridge between both electrodes (*e.g.* by tunnelling between the particles). As these particles are subject to a reduced but still active driving force for further electrochemical reactions, larger particles can consume smaller ones and eventually break the electronic path. This will then lead to an instable ON state during electrical biasing.

It is intriguing that quite large particles can be formed within the switching material matrix. A closer look at the filament particles reveals a stress induced contradiction of the crystal lattices. Fig. 5 shows an exemplary higher resolution TEM image of an embedded Ag nanoparticle in the oxide matrix as well as the corresponding line scan and FFT spectrum. The lattice spacing from the line scan and FFT spectrum

is $d_{hkl} = 0.234$ nm, corresponding to a lattice constant of $a \approx 0.405$ nm. Compared to the bulk lattice constant ($a_0 = 0.4079$ nm)⁴² this corresponds to a contraction of $\Delta a/a_0 = -2.1 \times 10^{-3}$ to -7×10^{-2} (on average $\langle \Delta a/a_0 \rangle = -2.6 \times 10^{-2} \pm 0.023$) for all measured particles. Given the compressibility of Ag, $\kappa = 9.93 \times 10^{-12} \text{ m}^2 \text{ N}^{-1}$, and the average particle radius $\langle r \rangle$ (*i.e.* here $\langle r \rangle = 7.4$ nm), the interfacial stress is³⁰

$$f = -\frac{3r\Delta a}{2a_0\kappa} \approx 29 \frac{N}{m} \quad (2)$$

This is about six times higher than what has been reported by Hofmeister *et al.* ($f = 4.7 \text{ N m}^{-1}$) for ion implanted Ag nano-clusters in a glassy soda-lime matrix (72 mol% SiO_2 and 13.8 mol% Na_2O).⁴³ Dubiel *et al.* previously contributed higher stress to a weaker metal-oxide interaction.⁴⁴ Smaller particles (as those ion implanted studied by Hofmeister *et al.*) have larger surface to volume ratios and therefore a stronger metal-oxide interaction as the larger particles formed during switching, which additionally may be found in voids/holes of the sputtered oxide. We therefore believe that the higher interfacial stress we observe (on average) is due to the larger size of the particles, potentially formed during switching in voids/holes, which have weaker metal-oxide interactions. In general, the interfacial stress may be determined by the chemical composition of the switching and active material to some degree. But importantly for nanoscale devices it may be mainly affected by the material morphology (*e.g.* porosity or interfacial stress to the substrate or inert electrode). The latter typically depends on the fabrication process such as sputtering, evaporation or atomic layer deposition.

When comparing PMMA with SiO_2 , an argument for the large filaments observed in PMMA could be its smaller Young's modulus of about $E = 3$ GPa (ref. 45) compared to oxides like SiO_2 ($E = 73$ GPa (ref. 46)). In fact, for SiO_2 we observe (denser) filaments with a diameter of 60 nm or below. Nevertheless, it should be noted that from the TEM images those filaments appear to be rather clusters of nanoparticles than thick and continuous nanowires. A similar situation may be true for PMMA. However, PMMA samples could not be analysed by TEM as the PMMA layer is too thick (about 180 nm) and leads to significant carbon contamination. It is further worth to mention that both in PMMA and SiO_2 , stress is decreased by incorporation of water.^{45,47} Smaller stress could make it easier to grow a metal filament within the switching material, and hence, reduce the switching voltage in ambient atmosphere as previously reported.⁴⁸⁻⁵⁰ In high vacuum conditions, switching may be therefore not only suppressed by the lack of ambient humidity^{38,51} which supplies counter charges,⁵⁰ but also by higher stress in the switching material. The interfacial stress of particles could be reduced by doping the oxide with fluorine as $\text{Si}(\text{-F})_2$ bonds allow higher water absorption.³⁷ As previously mentioned this could be a strategy to overcome the problem of nanoparticles remaining in the oxide during RESET as well. We suggest the stress situation inside the switching material matrix during filament growth should be analysed in future studies with particular attention

to the impact of the atmosphere during switching. The lateral structures we used have an ideal geometry to study such effects as they allow TEM analysis with high resolution and device dimensions nearly comparable to those found in many vertical devices.

Conclusions

We studied lateral and vertical CBRAM model devices that allow us to systematically relate important switching properties and their statistics to a direct characterisation of their critical switching region by SEM and TEM. We identified different limiting regimes *via* Weibull slopes in the switching statistics, and link this to multiple filament formation. We propose that the partial dissolution of the active electrode material is responsible for a change in switching conditions from cycle to cycle, resulting in different filament nucleation sites, *i.e.* multiple filaments. Our TEM analysis revealed that a filament is composed of metallic clusters rather than a continuous metal nanowire. These clusters are not completely removed from the switching material matrix upon RESET and appear to grow by consumption of smaller clusters. The formation of clusters is thereby promoted by a dynamic interplay of the cation mobility and redox rate during switching. We further estimated the mechanical stress of the nanoparticles within the switching material. We measured a lattice contraction below 3% and interfacial stress much higher to what has been previously reported for ion implanted Ag nanoparticles in a glassy matrix. We attribute the higher interfacial stress to weaker metal-oxide interactions as the nanoparticles are most likely formed in holes and voids of the switching material matrix. In high vacuum conditions or non-ambient conditions, switching may be therefore not only suppressed by the lack of ambient humidity which supplies counter charges, but also by higher stress in the switching material.

Since the classical growth model for filaments in ECM cells fails to capture the observed filament dynamics, we suggest a new categorization framework for ECM cells, as depicted in Fig. 7. The main distinguishing feature is whether the chemical nature or the morphology of the electrolyte (*i.e.* switching material) is dominating the switching process. In the first case, we expect a rather continuous classical shape of the filament (similar to a nanowire or conical shape), whereas in the latter case the formation of metal clusters may become kinetically more favourable. The interplay between (local) chemistry, morphology, interfacial stress and dynamic effects of these three properties have not been combined in a single framework for modelling the filament growth yet.

Historically, the filament growth in ECM cells was inspired by the growth of metal filaments in liquids. An exemplary model system is Ag/H₂O/Pt, where tree-like filaments are observed from the counter electrode (Pt) towards the active electrode (Ag).⁵² The liquid allows for a high degree of mechanical freedom and low interfacial stress compared to metal inclusions in solids. In this first type of ECM system, the

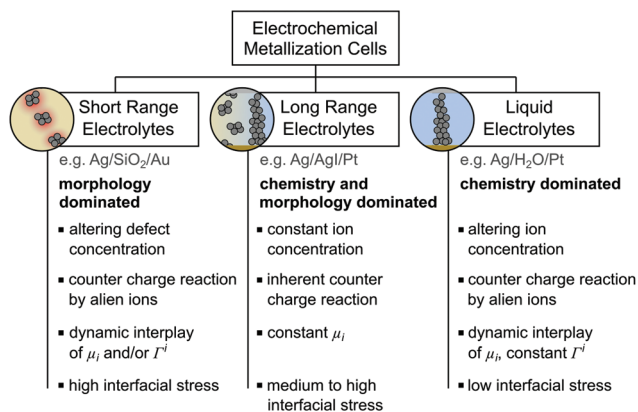


Fig. 7 Proposed categorization of Electrochemical Metallization Cells. The filament growth in liquid electrolytes such as the Ag/H₂O/Pt⁵² system is dominated by the chemistry of the electrolyte and obeys the classical electrochemical growth model. Solid ECM cells may be distinguished in having long or short range electrolytes, respectively. In long range electrolytes ionic conductivity is a macroscopic material behaviour. In the solid state, both the chemistry and morphology of long range electrolytes affect the filament growth. Short range electrolytes show some ionic conductivity on the nanoscale and the morphology of the electrolyte is dominating the switching.

chemistry of the electrolyte dominates the switching process. In comparatively low concentrated solutions with high ion concentration gradients (high concentration at the active electrode, low concentration at the counter electrode) the counter charge reaction to keep charge neutrality⁵⁰ will be driven by alien ions such as OH⁻. The ionic concentration (and hence ion mobility) can change during device operation similar to the dissolution of salts in liquids, whereas the redox rate is mainly given by the reduction at the counter electrode (*i.e.* nearly no reduction in the liquid). Thus, we also assume a dynamic interplay of μ_i and Γ^i . However, Γ^i will be always less dominating in the liquid compared to μ_i , and hence, tree-like filaments are formed.

For more complex solid ECM cells we distinguish two cases. ECM cells based on long range electrolytes are classical solid electrolytes where ion conductivity is a macroscopic material behaviour. A number of these materials, in particular AgI,¹⁴ do not allow for a variation of the stoichiometry, and hence, the ion concentration is chemically fixed and homogenous across the electrolyte. As a consequence, the cations of the electrolyte matrix (*i.e.* Ag⁺ for AgI) are inherently available at the counter electrode and act as counter charge during device operation. This classification has been discussed previously by Valov *et al.*^{39,53–55} Since the ion concentration is fixed, μ_i is fixed as well. As an extension of Valov *et al.*'s classification our model proposes, however, that the redox rate may depend (dynamically) on the morphology of the solid. We assume a local variation of Γ^i in polycrystalline or amorphous solids and practically homogenous Γ^i in single crystals. As a consequence, not only the chemistry of the electrolyte (*i.e.* ion concentration and mobility) but also the morphology (*e.g.* crystallinity, voids and holes) affect the filament growth. Both the morphology and

the chemical interaction of the electrolyte with the filament atoms result in medium to high interfacial stress which is larger compared to liquid systems (but smaller than for particles embedded in materials like oxides). Therefore, in long range electrolytes either continuous filaments or the formation of metal clusters during filament growth may be observed depending whether the chemistry or morphology are dominating the switching process. The filament growth direction will depend on whether μ_i or I^i is dominating, but the growth behaviour will not change during device operation for $\mu_i = \text{const}$.

For the second type of solid ECM cells the morphology is dominating the switching process. Materials like SiO_2 or PMMA, which are usually not considered to be electrolytes in a classical view, only show ionic behaviour on the nanoscale. Some other materials like Ag-doped GeS also fit into this category as they allow a change of the defect concentration over a wide range. We assume the local chemical behaviour depends on the device operation as well as the local morphology (e.g. a homogenous solid matrix will be chemically different from a matrix with voids and holes). Our model proposes a dynamic interplay during device operation between the defect concentration and redox rate as both are inhomogeneous across the electrolyte (in time and spatially). As a consequence of the inhomogeneous defect concentration, the counter charge is supplied by alien ions, similar to liquid systems. In contrast to classical ion conductors we assume a higher interfacial stress due to weaker interactions between the filament atoms and the switching material. However, more detailed research for other materials is required here to validate our assumptions. As a result of these properties we believe that the morphology of the switching material is the dominating factor for the switching process. Therefore, we assume that the formation of metal clusters and particles is energetically more favourable compared to the formation of continuous nanowires. However, it should be noted that the particle size (here some tens of nanometres or even more) can be similar to the gap distance for comparatively small gap lengths.

For future device improvement, it is important to tune the dissolution of the filament particles upon RESET e.g. by doping the oxide with fluorine, to avoid a progressive accumulation of metal inclusions, which will result in eventual failure to switch OFF the device. Further attention needs to be paid to the partial dissolution of the active electrode material which can cause different switching conditions for subsequent cycles and results in statistical variability of the switching voltages.

Conflicts of interest

There are no conflicts to declare.

Acknowledgements

The authors acknowledge Richard Langford, Jon J. Rickard and Eric Tapley (Cavendish Laboratory, University of

Cambridge) for their support in SEM and TEM. This work has been financially supported by ERC grant InsituNANO 279342 and a DFG research fellowship under grant TA 1122/1-1.

Notes and references

- 1 International Technology Roadmap for Semiconductors (ITRS), 2013, <http://www.itrs2.net/>.
- 2 D. J. Wouters, R. Waser and M. Wuttig, Phase-Change and Redox-Based Resistive Switching Memories, *Proc. IEEE*, 2015, **103**, 1274–1288.
- 3 S. Menzel, U. Böttger, M. Wimmer and M. Salinga, Physics of the Switching Kinetics in Resistive Memories, *Adv. Funct. Mater.*, 2015, **25**, 6306–6325.
- 4 V. Jousseume, J. Buckley, Y. Bernard, P. Gonon, C. Vallee, M. Mougnot, H. Feldis, S. Minoret, G. Chamot-Maitral and A. Persico, *et al.*, Back-End-of-Line Integration Approaches for Resistive Memories, *IEEE International Interconnect Technology Conference*, 2009, pp. 41–43.
- 5 J. Borghetti, G. S. Snider, P. J. Kuekes, J. J. Yang, D. R. Stewart and R. S. Williams, “Memristive” Switches Enable “stateful” Logic Operations via Material Implication, *Nature*, 2010, **464**, 873–876.
- 6 E. Linn, R. Rosezin, S. Tappertzhofen, U. Böttger and R. Waser, Beyond von Neumann–Logic Operations in Passive Crossbar Arrays alongside Memory Operations, *Nanotechnology*, 2012, **23**, 305205.
- 7 M. Cassinerio, N. Ciocchini and D. Ielmini, Logic Computation in Phase Change Materials by Threshold and Memory Switching, *Adv. Mater.*, 2013, **25**, 5975–5980.
- 8 D. Ielmini, Filamentary-Switching Model in RRAM for Time, Energy and Scaling Projections. *IEEE International Electron Devices Meeting*, 2011, pp. 17.2.1–17.2.4.
- 9 T. Ohno, T. Hasegawa, T. Tsuruoka, K. Terabe, J. K. Gimzewski and M. Aono, Short-Term Plasticity and Long-Term Potentiation Mimicked in Single Inorganic Synapses, *Nat. Mater.*, 2011, **10**, 591–595.
- 10 S. Cho, C. Yun, S. Tappertzhofen, A. Kursumovic, S. Lee, P. Lu, Q. Jia, M. Fan, J. Jian, H. Wang, *et al.*, Self-Assembled Oxide Films with Tailored Nanoscale Ionic and Electronic Channels for Controlled Resistive Switching, *Nat. Commun.*, 2016, **7**, 12373.
- 11 D. S. Jeong, R. Thomas, R. S. Katiyar, J. F. Scott, H. Kohlstedt, A. Petraru and C. S. Hwang, Emerging Memories: Resistive Switching Mechanisms and Current Status, *Rep. Prog. Phys.*, 2012, **75**, 76502.
- 12 Y. Yang and W. Lu, Nanoscale Resistive Switching Devices: Mechanisms and Modeling, *Nanoscale*, 2013, **5**, 10076.
- 13 C. Schindler, G. Staikov and R. Waser, Electrode Kinetics of Cu– SiO_2 -Based Resistive Switching Cells: Overcoming the Voltage-Time Dilemma of Electrochemical Metallization Memories, *Appl. Phys. Lett.*, 2009, **94**, 72109.
- 14 X. F. Liang, Y. Chen, L. Shi, J. Lin, J. Yin and Z. G. Liu, Resistive Switching and Memory Effects of AgI Thin Film, *J. Phys. D: Appl. Phys.*, 2007, **40**, 4767–4770.

- 15 K. Krishnan, M. Muruganathan, T. Tsuruoka, H. Mizuta and M. Aono, Highly Reproducible and Regulated Conductance Quantization in a Polymer-Based Atomic Switch, *Adv. Funct. Mater.*, 2017, 1605104.
- 16 J. van den Hurk, I. Valov and R. Waser, Preparation and Characterization of GeSx Thin-Films for Resistive Switching Memories, *Thin Solid Films*, 2013, 527, 299–302.
- 17 I. Valov and M. N. Kozicki, Cation-Based Resistance Change Memory, *J. Phys. D: Appl. Phys.*, 2013, 46, 74005.
- 18 S. Lin, L. Zhao, J. Zhang, H. Wu, Y. Wang, H. Qian and Z. Yu, Electrochemical Simulation of Filament Growth and Dissolution in Conductive-Bridging RAM (CBRAM) with Cylindrical Coordinates. *IEEE International Electron Devices Meeting*, 2012, pp. 26.3.1–26.3.4.
- 19 S. Menzel, P. Kaupmann and R. Waser, Understanding Filamentary Growth in Electrochemical Metallization Memory Cells Using Kinetic Monte Carlo Simulations, *Nanoscale*, 2015, 7, 12673–12681.
- 20 S. Menzel, I. Valov, R. Waser, B. Wolf, S. Tappertzhofen and U. Bottger, Statistical Modeling of Electrochemical Metallization Memory Cells, *IEEE International Memory Workshop*, 2014, pp. 1–4.
- 21 C. Hsiung, H.-W. Liao, J.-Y. Gan, T.-B. Wu, J.-C. Hwang, F. Chen and M.-J. Tsai, Formation and Instability of Silver Nanofilament in Ag-Based Programmable Metallization Cells, *ACS Nano*, 2010, 4, 5414–5420.
- 22 Y. Yang, P. Gao, S. Gaba, T. Chang, X. Pan and W. Lu, Observation of Conducting Filament Growth in Nanoscale Resistive Memories, *Nat. Commun.*, 2012, 3, 732.
- 23 W. A. Hubbard, E. R. White, A. Kerelsky, J. J. Lodico and B. C. Regan, In Situ STEM of Ag and Cu Conducting Bridge Formation through Al₂O₃ in Nanoscale Resistive Memory Devices, *Microsc. Microanal.*, 2014, 20, 1550–1551.
- 24 Y. Yang, P. Gao, L. Li, X. Pan, S. Tappertzhofen, S. Choi, R. Waser, I. Valov and W. D. Lu, Electrochemical Dynamics of Nanoscale Metallic Inclusions in Dielectrics, *Nat. Commun.*, 2014, 5, 4232.
- 25 G. Di Martino, S. Tappertzhofen, S. Hofmann and J. Baumberg, Nanoscale Plasmon-Enhanced Spectroscopy in Memristive Switches, *Small*, 2016, 12, 1334–1341.
- 26 Z. Wang, S. Joshi, S. E. Savel'ev, H. Jiang, R. Midya, P. Lin, M. Hu, N. Ge, J. P. Strachan, Z. Li, *et al.*, Memristors with Diffusive Dynamics as Synaptic Emulators for Neuromorphic Computing, *Nat. Mater.*, 2017, 16, 101–108.
- 27 W. Weibull, A Statistical Distribution Function of Wide Applicability, *J. Appl. Mech.*, 1951, 18, 293–297.
- 28 S. Tappertzhofen, *Redox and Mass Transport Phenomena in Resistively Switching Thin Films*, PhD Thesis, RWTH Aachen University, Dr Hut Verlag, Munich, 2014, ISBN: 978-3-8439-1832-9.
- 29 S. Tappertzhofen, E. Linn, U. Bottger, R. Waser and I. Valov, Nanobattery Effect in RRAMs - Implications on Device Stability and Endurance, *IEEE Electron Device Lett.*, 2014, 35, 208–210.
- 30 B. Medasani, Y. H. Park and I. Vasiliev, Theoretical Study of the Surface Energy, Stress, and Lattice Contraction of Silver Nanoparticles, *Phys. Rev. B: Condens. Matter*, 2007, 75, 235436.
- 31 S. Menzel, U. Böttger and R. Waser, Simulation of Multilevel Switching in Electrochemical Metallization Memory Cells, *J. Appl. Phys.*, 2012, 111, 14501.
- 32 M. Kund, G. Beitel, C.-U. Pinnow, T. Rohr, J. Schumann, R. Symanczyk, K. Ufert and G. Muller, Conductive Bridging RAM (CBRAM): An Emerging Non-Volatile Memory Technology Scalable to Sub 20 nm. *IEEE International Electron Devices Meeting*, 2005, pp. 754–757.
- 33 X. Tian, L. Wang, J. Wei, S. Yang, W. Wang, Z. Xu and X. Bai, Filament Growth Dynamics in Solid Electrolyte-Based Resistive Memories Revealed by in Situ TEM, *Nano Res.*, 2014, 7, 1065–1072.
- 34 R. Waser, R. Dittmann, G. Staikov and K. Szot, Redox-Based Resistive Switching Memories - Nanoionic Mechanisms, Prospects, and Challenges, *Adv. Mater.*, 2009, 21, 2632–2663.
- 35 S. Tappertzhofen, H. Mündelein, I. Valov and R. Waser, Nanoionic Transport and Electrochemical Reactions in Resistively Switching Silicon Dioxide, *Nanoscale*, 2012, 4, 3040.
- 36 T. Tsuruoka, I. Valov, S. Tappertzhofen, J. van den Hurk, T. Hasegawa, R. Waser and M. Aono, Redox Reactions at Cu_xAg/Ta₂O₅ Interfaces and the Effects of Ta₂O₅ Film Density on the Forming Process in Atomic Switch Structures, *Adv. Funct. Mater.*, 2015, 25, 6374–6381.
- 37 H. Miyajima, R. Katsumata, Y. Nakasaki, Y. Nishiyama and N. Hayasaka, Water Absorption Properties of Fluorine-Doped SiO₂ Films Using Plasma-Enhanced Chemical Vapor Deposition, *Jpn. J. Appl. Phys.*, 1996, 35, 6217–6225.
- 38 T. Tsuruoka, I. Valov, C. Mannequin, T. Hasegawa, R. Waser and M. Aono, Humidity Effects on the Redox Reactions and Ionic Transport in a Cu/Ta₂O₅/Pt Atomic Switch Structure, *Jpn. J. Appl. Phys.*, 2016, 55, 06GJ09.
- 39 I. Valov, E. Linn, S. Tappertzhofen, S. Schmelzer, J. van den Hurk, F. Lentz and R. Waser, Nanobatteries in Redox-Based Resistive Switches Require Extension of Memristor Theory, *Nat. Commun.*, 2013, 4, 1771.
- 40 A. Schröder, J. Fleig, J. Maier and W. Sitte, Inherent Emf Relaxation of Electrochemical Cells with Nanocrystalline Ag Electrodes, *Electrochim. Acta*, 2006, 51, 4176–4181.
- 41 D. Ielmini, R. Bruchhaus and R. Waser, Thermochemical Resistive Switching: Materials, Mechanisms, and Scaling Projections, *Phase Transitions*, 2011, 84, 570–602.
- 42 W. P. Davey, Precision Measurements of the Lattice Constants of Twelve Common Metals, *Phys. Rev.*, 1925, 25, 753–761.
- 43 H. Hofmeister, S. Thiel, M. Dubiel and E. Schurig, Synthesis of Nanosized Silver Particles in Ion-Exchanged Glass by Electron Beam Irradiation, *Appl. Phys. Lett.*, 1997, 70, 1694.
- 44 M. Dubiel, H. Hofmeister and E. Schurig, Compressive Stresses in Ag Nanoparticle Doped Glasses by Ion Implantation, *Phys. Status Solidi*, 1997, 203, R5–R6.

- 45 C. Ishiyama and Y. Higo, Effects of Humidity on Young's Modulus in Poly(methyl Methacrylate), *J. Polym. Sci., Part B: Polym. Phys.*, 2002, **40**, 460–465.
- 46 B. J. Mrstik, A. G. Revesz, M. Ancona and H. L. Hughes, Structural and Strain-Related Effects during Growth of SiO₂ Films on Silicon, *J. Electrochem. Soc.*, 1987, **134**, 2020.
- 47 I. Blech and U. Cohen, Effects of Humidity on Stress in Thin Silicon Dioxide Films, *J. Appl. Phys.*, 1982, **53**, 4202.
- 48 N. Knorr, R. Wirtz, S. Rosselli and G. Nelles, Field-Absorbed Water Induced Electrochemical Processes in Organic Thin Film Junctions, *J. Phys. Chem. C*, 2010, **114**, 15791–15796.
- 49 T. Tsuruoka, K. Terabe, T. Hasegawa, I. Valov, R. Waser and M. Aono, Effects of Moisture on the Switching Characteristics of Oxide-Based, Gapless-Type Atomic Switches, *Adv. Funct. Mater.*, 2012, **22**, 70–77.
- 50 S. Tappertzhofen, I. Valov, T. Tsuruoka, T. Hasegawa, R. Waser and M. Aono, Generic Relevance of Counter Charges for Cation-Based Nanoscale Resistive Switching Memories, *ACS Nano*, 2013, **7**, 6396–6402.
- 51 S. Tappertzhofen, M. Hempel, I. Valov and R. Waser, Proton Mobility in SiO₂ Thin Films and Impact of Hydrogen and Humidity on the Resistive Switching Effect, *Mater. Res. Soc. Symp. Proc.*, 2011, **1330**, 1–6.
- 52 X. Guo, C. Schindler, S. Menzel and R. Waser, Understanding the Switching-off Mechanism in Ag⁺ Migration Based Resistively Switching Model Systems, *Appl. Phys. Lett.*, 2007, **91**, 133513.
- 53 I. Valov, S. Tappertzhofen, E. Linn, S. Menzel, J. van den Hurk and R. Waser, (Keynote) Atomic Scale and Interface Interactions in Redox-Based Resistive Switching Memories, *ECS Trans.*, 2014, **64**, 3–18.
- 54 D.-Y. Cho, S. Tappertzhofen, R. Waser and I. Valov, Chemically-Inactive Interfaces in Thin Film Ag/AgI Systems for Resistive Switching Memories, *Sci. Rep.*, 2013, **3**, 1169.
- 55 D.-Y. Cho, I. Valov, J. van den Hurk, S. Tappertzhofen and R. Waser, Direct Observation of Charge Transfer in Solid Electrolyte for Electrochemical Metallization Memory, *Adv. Mater.*, 2012, **24**, 4552–4556.